Cross-diffusion induced convective patterns in microemulsion systems

M. A. Budroni,[a] L. Lemaigre,[b] A. De Wit[b] and F. Rossi*[c]

Received Xth XXXXXXXXXX 20XX, Accepted Xth XXXXXXXXX 20XX
First published on the web Xth XXXXXXXXXX 200X
DOI: 10.1039/b000000x

Cross-diffusion phenomena are shown experimentally to be able to induce convective fingering around an initially stable stratification of two microemulsions having a different composition. Upon diffusion of a salt entraining water and AOT micelles by cross-diffusion, the miscible interface deforms into fingers following the build-up of a non monotonic density profile in the gravitational field. A diffusion model incorporating cross-diffusion effects provides an explanation for the mechanism of the buoyancy-driven hydrodynamic instability and the properties of the convective fingers.

1 Introduction

Cross-diffusion, whereby a flux of a given species entrains the diffusive transport of another species, has recently been shown to trigger a wealth of new pattern formation dynamics in reaction-diffusion (RD) systems. In particular, the influence of cross-diffusion on RD Turing and wave instabilities has been studied both theoretically [1–6] and experimentally [7]. Typical systems in which cross-diffusion driven reactive patterns can be studied are AOT (sodium bis(2-ethylhexyl)sulfosuccinate Aerosol OT) micelles where a large number of RD patterns have been characterized [8] and the diffusion matrix often contains large off-diagonal terms [9–12].

Cross-diffusion effects are also known to be able to trigger convective motions around liquid interfaces in the absence of chemical reactions. Experimental studies of a ternary system, polyvinylpyrrolidone(PVP)/dextran/H_2O [13], have indeed demonstrated hydrodynamic instabilities at the miscible interface between non reactive solutions exhibiting large cross-diffusion properties. Specifically, the development of convective fingers was observed when an aqueous solution of dextran was placed above a denser aqueous solution of equimolar dextran containing polyvinylpyrrolidone (PVP). Starting from an initially stable density stratification, the diffusion of PVP from the lower solution to the upper one generates a co-flux of dextran. In turn, this cross-diffusion effect causes an inversion of the density profile at the miscible interface and the appearance of the convective fingers. This system and new variants with other polymers than PVP have been thoroughly investigated both experimentally and theoretically [14–17]. Subsequently, the effect of additives on the PVP/dextran/H_2O system was investigated in more detail [18–20]. From a theoretical perspective, a general theoretical framework of the stability conditions of miscible interfaces with regard to buoyancy-driven convection in the presence of cross-diffusion effects has been developed [21]. However, only a limited number of systems were investigated experimentally and, in all of them, cross-diffusion was generated by the flux of large polymers and molecules *i.e.* by an excluded volume effect.

Cross-diffusion effects are thus known to yield a large variety of pattern-forming instabilities either when coupled to reactive processes like in AOT microemulsions or when they influence density profiles and trigger convection as in polymeric systems. It is likely that both reactive and convective effects should be able to interact, giving rise to a wealth of possible reaction-diffusion-convection (RDC) patterns and instabilities to be studied. To open such perspectives, it is important to first have a model system in which both RD and convective instabilities are well documented separately. In this context, it is of interest to check whether the cross-diffusion driven convective fingering studied in polymers can also be obtained in AOT microemulsions, for which the diffusion matrix also often contains large off-diagonal terms, and if so, what are their properties.

Here we investigate the properties of hydrodynamic convective patterns triggered by cross-diffusion in microemulsions in the absence of any reaction. In particular, we characterise experimentally the fingered convective motions growing in time at the interface between two identical H_2O/AOT/octane water-in-oil reverse microemulsions (AOT-ME) in a gravitational field, when the lower denser solution contains a simple water-soluble molecule ($NaBrO_3$) free to diffuse towards the upper

[a] *Department of Chemistry and Pharmacy, University of Sassari, Via Vienna 2, 07100 Sassari, Italy.*
[b] *Nonlinear Physical Chemistry Unit, Service de Chimie Physique et Biologie Théorique, Université libre de Bruxelles, CP 231 - Campus Plaine, 1050 Brussels, Belgium.*
[c] *Department of Chemistry and Biology, University of Salerno Via Giovanni Paolo II 132, 84084 Fisciano (SA), Italy; E-mail: frossi@unisa.it*

less dense layer (see Fig.1). We develop a theoretical model to connect the dynamic development of the pattern to the spatio-temporal evolution of the density profile in the system. Good qualitative agreement between the instability scenarios predicted by the theory and the experimentally observed convective pattern is obtained. As the microemulsion system under study here is known to exhibit a large variety of patterns where cross-diffusion may couple to reaction processes [7], our results provide characterisation of a good candidate for future studies of cross-diffusion-driven RDC instabilities. In the next sections, we introduce the cross-diffusive properties of AOT microemulsions and describe the experimental methods. The experimental results are presented in section 4 and interpreted by means of numerical calculations. Conclusions are outlined in section 5.

2 Cross-diffusion in microemulsions

In multicomponent solutions (multiple solutes in a solvent), diffusion processes can be described by Fick's law generalized to an n-component system $f_i = -\sum_{j=1}^{n-1} D_{ij} \nabla c_j$, where the flux f_i of species i depends on the concentration gradients of all the other species. D_{ii} represent the diagonal terms of the diffusion matrix and are called *main* terms, while the off-diagonal elements D_{ij} are known as *cross-diffusion* coefficients. Thus, in an n-component system ($n-1$ solutes plus the solvent), the diffusion matrix has $(n-1)^2$ elements: $n-1$ main terms and $(n-1)(n-2)$ cross-diffusion terms. The sign of the cross-diffusion terms can be either positive (*co*-flux) or negative (*counter*-flux), depending on the type of interactions involving the solutes. Among others, three important mechanisms in which cross coefficients can be quite large (even larger than the main terms) are electrostatic interactions, excluded volume effects, and complexation. [22]

As in polymers, excluded volume mechanisms can be particularly important in microemulsions, even though further mechanisms related with the size of the water droplets are at play [10,12]. A microemulsion is a thermodynamically stable dispersion of two immiscible liquids in the presence of a surfactant. Their properties as a two-fold solvent, both for hydrophilic and hydrophobic species, are useful for many applications, including pollution remediation, drug delivery and the synthesis of nano-materials [23]. Many physical properties (such as conductivity and viscosity) of the AOT-ME show a threshold-like dependence on ϕ_d, the volume fraction of the dispersed phase ($\phi_d = \phi_{H_2O} + \phi_{AOT}$). This dependence is due to percolation. If $\phi_d << \phi_{cr}$ (percolation threshold, $\phi_{cr} \simeq 0.5 - 0.6$) [8,24], the microemulsion can be accurately characterized as a medium in which water droplets float freely. The radius of a droplet's water core in nanometers is roughly given by $r = 0.17\omega$, where ω=[H_2O]/[AOT]; r is independent of the octane volume fraction in the microemulsion. The total radius of the droplet plus the surrounding AOT monolayer (hydrodynamic radius), r_d, exceeds r by the length of an AOT molecule ($\simeq$ 1.1 nm). [25,26]

Measurements of cross-diffusion coefficients in ternary AOT microemulsions (H_2O (1) / AOT (2) / oil) revealed that the cross-diffusion coefficient D_{12}, which describes the flux of water induced by a gradient in the surfactant concentration, can be significantly larger than both D_{11} and D_{22}, i.e. the main diffusion coefficients of water and AOT, respectively [9,10]. The ratio D_{12}/D_{22} increases with the mean radius r of the water droplets. Large co-fluxes of H_2O and AOT can also be induced by a water soluble species in quaternary systems H_2O (1) / AOT (2) / additive (3) / octane, where D_{13} and D_{23} were found to be large and positive [11,12]. AOT micro emulsions are thus typical systems in which cross-diffusion effects are the source of a large variety of pattern-forming instabilities. While this has already been largely demonstrated in RD conditions, let us now show that cross-diffusion can also trigger specific convective patterns in unreactive AOT systems.

3 Experimental Methods

The experimental setup (see Fig.1) consists of a specifically designed, vertically oriented, Hele-Shaw cell (two glass plates separated by a thin gap of 0.5 mm) filled with the solutions of interest [27]. Two microemulsions are layered in the Hele-Shaw cell: the bottom one (ME_B) contains the unreactive species $NaBrO_3$ in the water core of the droplets, and the top one (ME_T) does not. The two microemulsions have the same structural characteristics (*i.e.* same ω and ϕ_d), so that only $NaBrO_3$ exhibits a concentration gradient between the two layers. Water-in-oil microemulsions were prepared using distilled water, AOT (Aldrich) and octane (Sigma reagent grade). Octane was further purified by mixing with concentrated H_2SO_4 for four days. A stock solution of AOT in octane ([AOT] = 1.5 M) was prepared and diluted to the experimental values of ω and ϕ_d by adding water and an aqueous stock solution of $NaBrO_3$ 0.4 M (Sigma analytical grade). In the following, we will refer to the concentration of $NaBrO_3$ as the one in the water core of the microemulsions. All experiments were conducted at room temperature (∼21 °C) with [H_2O] = 3.58 M and [AOT] = 0.3 M, *i.e.* $\omega = 12$ and $\phi_d = 0.18$ and the concentration of $NaBrO_3$ was varied in the interval $0.1 \leq NaBrO_3 \leq 0.4$ M. Under these conditions the diffusion matrix of the microemulsions has been characterized in detail for the ternary system (H_2O (1) / AOT (2) / octane) [9–11], and for several additives in quaternary (H_2O (1) / AOT (2) / additive (3) / octane) [12] and pentanary systems (H_2O (1) / AOT (2) / additive1 (3) / additive2 (4) / octane) [7]. In particular, Table 1 reports the diffusion matrix **D** of a quaternary system where $NaBrO_3$ is the third component. Check experiments were also run by using the colored salts $KMnO_4$ or $K_2Cr_2O_7$

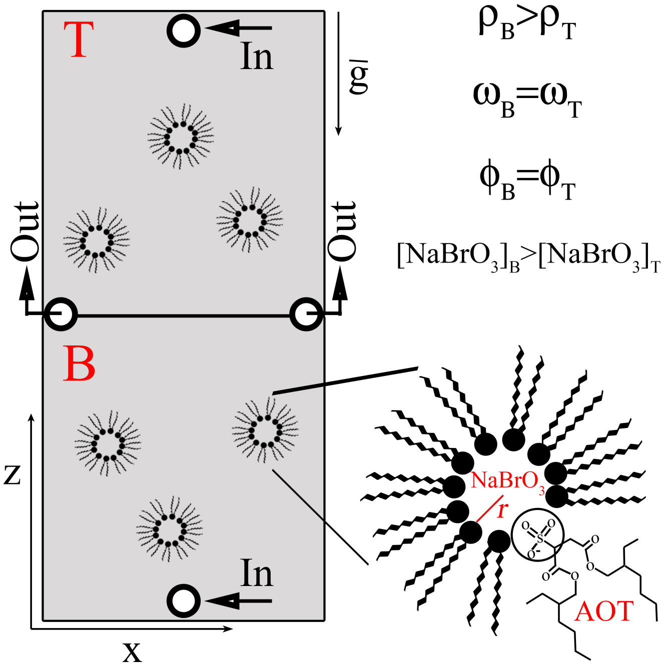

Fig. 1 Sketch of the experimental configuration.

in the place of $NaBrO_3$.
The two microemulsions were simultaneously pumped into

Table 1 Quaternary Diffusion Coefficients (in 10^{-6} cm^2/s) for the Water (1) / AOT (2) / $NaBrO_3$ (3) / Octane system when $\omega = 11.84$, $\phi_d = 0.18$

j	D_{j1}	D_{j2}	D_{j3}
1	(0.64 ± 0.5)	(7.1 ± 3)	(8.1 ± 1)
2	(-0.011 ± 0.002)	(1.5 ± 0.3)	(1.9 ± 0.06)
3	(-0.0031 ± 0.007)	(-0.073 ± 0.002)	(0.43 ± 0.06)

the cell, avoiding the formation of air bubbles, through the inlets positioned at the top and at the bottom of the reactor (see arrows "In" in Figure 1). The excess of solutions was pumped out through the cell's outlets (see arrows "Out" in Figure 1) until a flat interface between the two liquids was obtained; both the cell inlets and outlets were finally closed to avoid leakage. The dynamics at the interface was recorded with a commercial optical device implementing the Schlieren technique[28]. This technique allows one to visualize density gradients, thanks to changes in the refractive index and, hence, convective motions in colorless fluids.
The density of the microemulsions was measured at constant temperature (21.5°C) for different concentrations of $NaBrO_3$ at $\omega = 12$ and $\phi_d = 0.18$. Moreover, measurements were performed at different values of ω and ϕ_d in order to establish how the density varies with the concentrations of AOT and water. The solutal expansion coefficients thus obtained were used in the numerical calculations presented in section 4.2.

4 Results and Discussion

4.1 Convective patterns

Experimental measurements show a slight increase in the density of the solution when $NaBrO_3$ is added to the water-in-oil microemulsion. The initial stratification of same microemulsions with $NaBrO_3$ added in the lower layer (Fig. 1) is thus statically stable, the bottom layer being the denser one. Soon after contact, convective patterns develop in few minutes around the initial flat contact line. Fig. 2 shows the appearance of convective fingers, which grow upwards and downwards around the interface, in a system where $[NaBrO_3]_B = 0.1$ M and $[NaBrO_3]_T = 0$ M. Here we assume that the addition of the fourth component in the bottom layer does not change the structural parameters of the microemulsions[11]. The typical growth dynamics of a single finger can be followed and characterized from the space-time (ST) plot depicted in Fig.2f built along the vertical line in Fig.2a. The system was analyzed in the first 1500 s from the beginning of the experiments, when the fingers still grow almost vertically before being bent and distorted by their complex interactions. The ST plot reveals that the typical development of fingers is not symmetric with respect to the interface at all times. Indeed, upward growing fingers develop faster (~ 140 μm/min) than the ones growing downwards (~ 130 μm/min). However the maximum length reached in both directions after ~ 900 s, before the onset of the lateral flows, is the same (~ 1.8 mm).

As the magnitude of the cross-diffusion coefficients depends on the composition of the solution and on the gradient in the concentration of the solutes[12,22], the concentration of the salt in the bottom layer was varied in the range $0.1 \leq [NaBrO_3]_B \leq 0.4$ M to check its effect on the fingering dynamics. The response to such concentration changes was analyzed by means of the following characteristic parameters: the onset time t_0, which is defined as the induction time of the convective instability; the total mixing length l_m, which is the mean total length of the straight fingers; the finger growth rate v_m, which gives the averaged speed at which convective fingers develop; and, finally, the hydrodynamic wavelength λ_m, defined as the average distance between two consecutive fingers. t_0, l_m and v_m can be directly extrapolated from vertical space-time plots as in Fig. 2f, while values for λ_m are calculated by means of space-time plots stacked along the horizontal interface between the two layers (see dashed line in Fig.

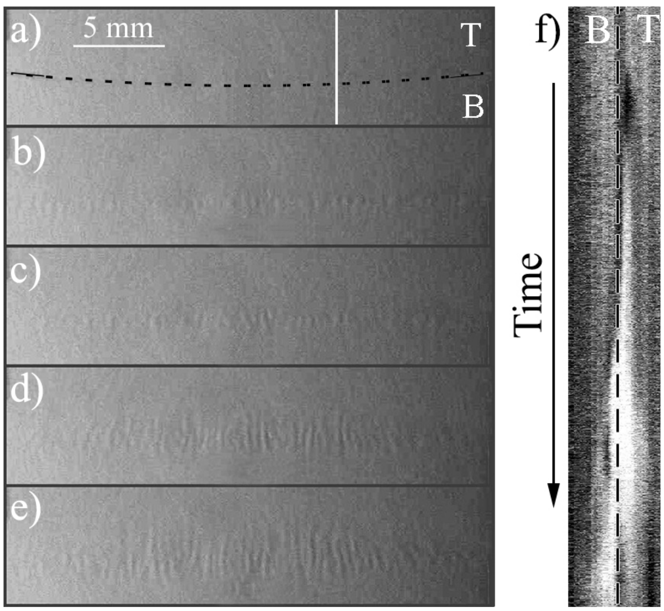

Fig. 2 a) – e) Development of the instability visualized by schlieren technique in a system where ω = 12, ϕ_d = 0.18 and $[NaBrO_3]_B$ = 0.1 M. The dashed line in panel a) indicates the initial interface between the two layers, top (T) and bottom (B). Snapshots are taken every 300 s. f) Space-time plot built along the vertical white line in panel a). Total time (vertical axis) is 1500 s. The horizontal length is 6 mm. The vertical dashed line indicates the interface between bottom (B) and top (T) layers.

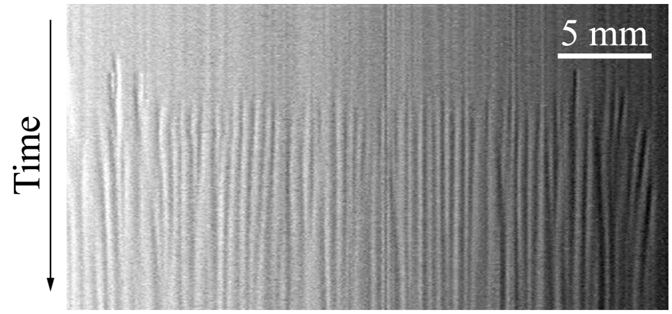

Fig. 3 ST plot built along the horizontal interface between the two layers of a system containing $[NaBrO_3]_B$ = 0.2 M at ω = 12, ϕ_d = 0.18.

2a). As an example, Fig. 3 shows the horizontal ST plot for a system containing $[NaBrO_3]_B$ = 0.2 M in the bottom layer. It can be noticed how the appearance of fingers is revealed by the vertical stripes which develop a few minutes after the two ME are put in contact. Because the gradients in the index of refraction tracked here are small, the experimental images are of low contrast. The extraction of the dynamical characteristics of the fingers from the space-time plots therefore suffered from an error larger than the errors in the physical parameters of the problem. Nevertheless we can get reliable and informative data which can be explained in the light of the theoretical description given in the next section. The typical dependences of the hydrodynamic features on $[NaBrO_3]_B$ are reported in Figure 4, where a decreasing trend can be seen for all the parameters.

The emergence of convective patterns cannot be attributed to surface tension-driven instability. As a matter of fact, the two layers in our system are completely miscible and there is no interfacial reaction which can promote the formation of surface tension gradients with the formation of new surface-active species. Indeed, the conditions for Marangoni instability are not met and local density changes along the gravitational field are solely responsible for the development of convective flows. Moreover, this buoyancy-driven instability cannot be due to a classical mechanism of double diffusion or diffusive layer convection[29–31], as there is no solute in the top emulsion that could trigger differential diffusion. Here, cross-diffusion phenomena have to be taken into account to explain the mechanism of the instability. Intuitively, the mechanism can be understood by bearing in mind that, in the presence of positive cross-diffusion coefficients like the ones in this microemulsion system, one species is able to generate a co-flux of the other solutes present in solution even if there is no gradient in their concentrations. In particular, a gradient in $[NaBrO_3]$ can trigger the motion of a large quantity of H_2O and AOT molecules since both the cross-diffusion terms D_{13} and D_{23} are large and positive (Table 1). Moreover, the mo-

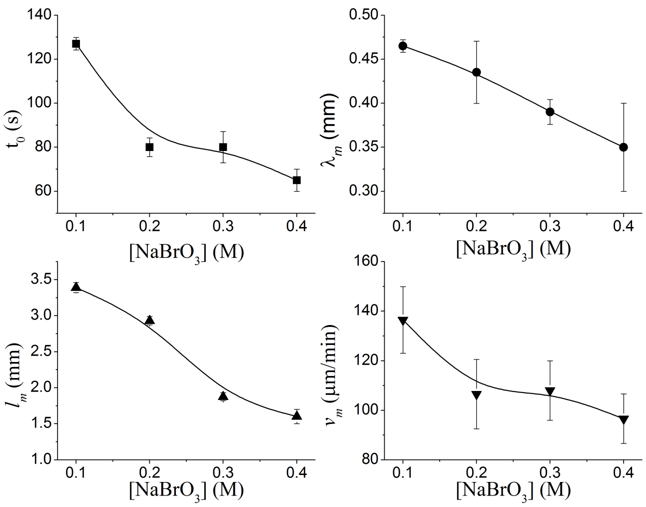

Fig. 4 Characteristic parameters of the fingering dynamics computed from experimental images. Solid lines are b-splines connecting the points, drawn to guide the eye.

tion of AOT generates, in turn, a further co-flux of H_2O (see D_{12}). Therefore, when $NaBrO_3$ diffuses from the bottom to the upper layer, it drags along both H_2O and AOT molecules thus generating a non-monotonic density distribution around the contact line, destabilizing an initially stable system.

At this stage it is not easy to understand the dependence of the hydrodynamic parameters upon $[NaBrO_3]_B$. However, we have to consider that the increase of the salt concentration causes two main effects in the system. On the one hand the density of the bottom layer increases and stabilizes the interface; on the other hand, the magnitude of the cross-diffusion coefficient changes in a non-trivial way[12,22]. Therefore the exact dependence of D_{ij} upon $[NaBrO_3]$ must be known in order to have a clearer picture of the system. Further insights into the instability mechanism can be drawn with a theoretical analysis of the system density profiles.

4.2 Theoretical interpretation of experimental scenarios

Density profiles for our ternary system can be reconstructed starting from Fick's equations with cross-diffusive terms explicitly included, *i.e.*

$$\partial_t A = D_{AA}\nabla^2 A + D_{AB}\nabla^2 B + D_{AC}\nabla^2 C \quad (1)$$
$$\partial_t B = D_{BA}\nabla^2 A + D_{BB}\nabla^2 B + D_{BC}\nabla^2 C \quad (2)$$
$$\partial_t C = D_{CA}\nabla^2 A + D_{CB}\nabla^2 B + D_{CC}\nabla^2 C \quad (3)$$

In equations (1–3) A, B, C represent the dimensional concentrations of H_2O, AOT and $NaBrO_3$ respectively; D_{II} are the main self-diffusion coefficients of the I–th species and D_{IJ} ($I \neq J$) define the cross-diffusivities of the I–th species with respect to the J–th solute. Although cross-diffusion coefficients depend on the chemical composition of the system, as a first approximation, we consider them here as constant[7].

In a 1D spatial domain of length L_z along the vertical z–axis, sketched in Fig.5, we consider a homogeneous initial distribution $A(z,0) = A_0, B(z,0) = B_0$, while a sharp initial gradient is imposed for the solute $C(z,t)$, according to the step function

$$C(z,0) = \begin{cases} C_0^B & \text{if } z \leq L_z/2 \\ C_0^T & \text{elsewhere} \end{cases}$$

This configuration describes a two-layer system: the upper layer (T) and the bottom layer (B), with composition (A_0, B_0, C_0^T) and (A_0, B_0, C_0^B), respectively. Upon contact, the two miscible solutions with different initial concentration of C start mixing by diffusion without affecting the thermal properties of the system.

The model equations can be conveniently cast into a dimensionless form by introducing a reference space scale, L_0, and the diffusive time scale, $t_0 = L_0^2/D_{CC}$. We can then define the dimensionless space and time variables $\zeta = z/L_0$ and $\tau = t/t_0$, respectively. If we scale the chemical concentrations as $(a,b,c) = (A - A_0, B - B_0, C - C_0^T)/\Delta C_0$, where $\Delta C_0 = C_0^B - C_0^T$, the dimensionless model reads

$$\partial_\tau a = \delta_{aa}\partial_\zeta^2 a + \delta_{ab}\partial_\zeta^2 b + \delta_{ac}\partial_\zeta^2 c \quad (4)$$
$$\partial_\tau b = \delta_{ba}\partial_\zeta^2 a + \delta_{bb}\partial_\zeta^2 b + \delta_{bc}\partial_\zeta^2 c \quad (5)$$
$$\partial_\tau c = \delta_{ca}\partial_\zeta^2 a + \delta_{cb}\partial_\zeta^2 b + \partial_\zeta^2 c \quad (6)$$

Here the dimensionless parameters $\delta_{ii} = D_{II}/D_{CC}$ are the ratios of the main molecular diffusion coefficients of the chemical solutes to that of species C, while $\delta_{ij} = D_{IJ}/D_{CC}$ are the ratios of the cross-diffusion coefficients of the chemical solutes to that of species C. In the dimensionless variables our problem is defined by the initial concentration profiles $a(\zeta,0) = b(\zeta,0) = 0$ and

$$c(\zeta,0) = \begin{cases} 1 & \text{if } \zeta \leq L_z/(2L_0) \\ 0 & \text{elsewhere} \end{cases}$$

With the assumption that the concentration of the chemical solutes changes only slightly with respect to the initial reference conditions (at least in the first phase of the diffusive process), the dimensionless density of the system at a certain time, $\rho(a,b,c,\zeta) = (\rho' - \rho^T)/(\rho^T \alpha_C \Delta C_0)$, can be expressed as a first order Taylor expansion of the concentrations as

$$\rho(a,b,c,\zeta) = R_a a(\zeta) + R_b b(\zeta) + c(\zeta) \quad (7)$$

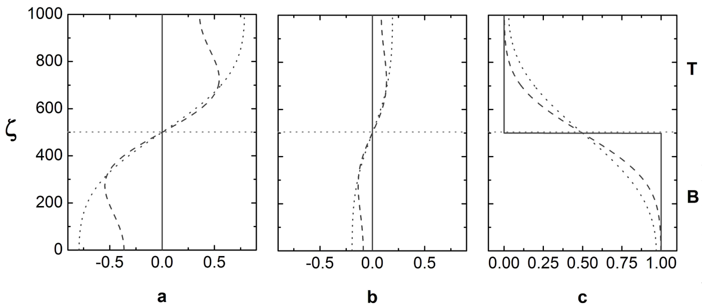

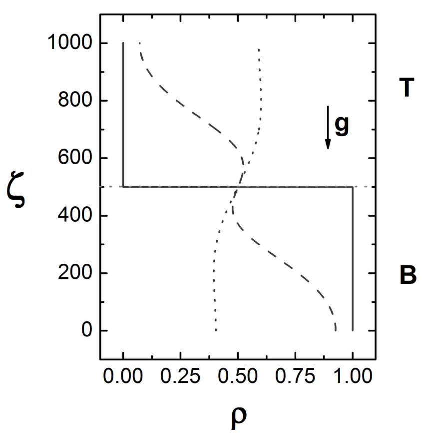

Fig. 5 Upper panel: From left to right, spatio-temporal evolution of *a*, *b* and *c* concentration profiles, respectively. In each panel solid curves describe the initial distribution of the species, while dashed and dotted profiles depict the concentration at time 2000 and 8000, respectively. Lower panel: spatio-temporal evolution of the related dimensionless density profile at time 0, 2000 and 8000. In each panel the horizontal dotted line at 500 space units represents the initial contact interface between the two layers.

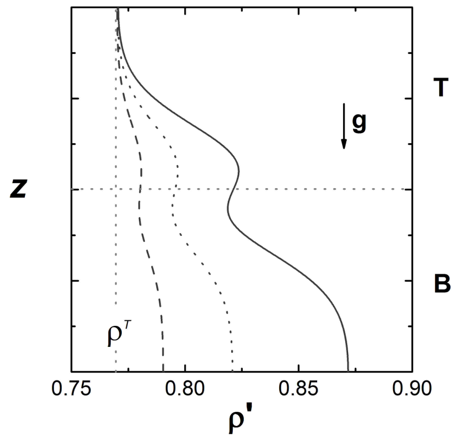

Fig. 6 Dimensional density profile at t = 2000 when the initial concentration jump ΔC_0 between the two layers is 0.2 M (dashed curve), 0.5 M (dotted curve) and 1.0 M (solid curve). The horizontal dotted line at 500 space units represents the initial contact interface between the two layers while the vertical dotted line at $\rho = 0.770$ g/cm^3 indicates the reference dimensional density of top layer, ρ^T.

where the buoyancy ratios $R_i = \alpha_I/\alpha_C$ control the relative contribution of the I–th species to the global density; $\alpha_C = \frac{1}{\rho^T}\frac{\partial \rho'}{\partial [C]}$ and $\alpha_I = \frac{1}{\rho^T}\frac{\partial \rho'}{\partial [I]}$ are the solutal expansion coefficients of C and the I–th solute, respectively; ρ^T is the dimensional density reference of the upper solution (A_0, B_0, C_0^T) and $\rho'(z,t)$ the dimensional density.

By introducing the solutions to the diffusion problem defined by eqs.(4–6), in equation (7), we can compute the spatio-temporal evolution of the dimensionless density profile. Although $\rho(a,b,c,\zeta)$ does not contain any extended information on the possible hydrodynamic patterns, since it cannot take into account the nonlinear coupling between convective flows and concentration fields, density profiles provide qualitative information on the instability scenarios to be expected. Indeed, hydrodynamic instabilities are typically expected in spatial domains where the density decreases along $\underline{g}$, as we then have a locally denser zone above a less dense one. Criteria for hydrodynamic instability are thus either (*i*) a monotonic downward decreasing density (with an absolute maximum in the upper layer) or (*ii*) non monotonic configurations with local maxima and minima so that, at least, in a local zone $\partial\rho/\partial\zeta < 0$.

We integrated numerically the equations (4–6) by using the Crank-Nicholson method, imposing no-flux boundary conditions at the borders of the spatial domain of length 1000 space units. Simulations are run for 10000 time units, using a spatial step $hx = 0.5$ and a time step $ht = 1 \times 10^{-3}$. The main parameters of the diffusion problem (δ_{ii}, δ_{ij}) are computed from

Table 2 Values for the self- and cross-diffusivity ratios, scaled by the sodium bromate self-diffusion coefficient.

Species j–th	δ_{aj}	δ_{bj}	δ_{cj}
H_2O a	1.515	16.512	18.837
AOT b	−0.021	3.491	4.419
$NaBrO_3$ c	−0.007	−0.170	1

Table 3 Values for the measured solutal expansion coefficients and related buoyancy ratios. $\rho^T = 0.770 \pm 0.003$ g/cm^3 is the density reference of the (A_0, B_0, C_0^T) solution.

Species (I)	$\frac{1}{\rho^T}\frac{\partial\rho'}{\partial[I]}$ at 21°C (M^{-1})	R_i
H_2O A	0.010 ± 0.002	0.050 ± 0.035
AOT B	0.3 ± 0.1	1.50 ± 1.25
$NaBrO_3$ C	0.2 ± 0.1	1

experimental data (see Table 1) and are listed with the buoyancy ratios R_i in Tables 2 and 3.

In Fig.5 we show the dimensionless concentration profiles of the species a, b and c at different times. The dynamics of species c features the classic flattening response of diffusive transport to an initial step concentration profile, according to the analytical solution $\frac{1}{2}\text{erf}(-\zeta/(2t)^{\frac{1}{2}})$. This behavior does not destabilize the system. However, as soon as c starts diffusing, it entrains a and b due to cross-diffusion. As a consequence, the initially homogeneous distributions of a and b become non-monotonic with a local mass accumulation and depletion just above and below the initial interface, respectively (see dashed curves in the first and second panels from the left in Fig.5). The transfer of a and b is sustained as long as the gradient of solute c is not completely smoothed out. It results in a final monotonic stratification in a and b on the upper layer, as described by the dotted curves in the first and second panels from the left of Fig.5. It is worth noticing that the effect of this process is much more significant for species a, which presents the highest cross-diffusion coefficient with the mass-driving species c.

As shown in the lower panel of Fig.5, the concentration dynamics influences the global dimensionless density profiles, constructed using eq.(7) and values of the buoyancy ratios in the ranges reported in Table 3. Within the large variance of the measured solutal expansion coefficients, a wide spectrum of morphologies of the density profiles can be found, included monotonically downward increasing density along the spatial axis, featuring hydrodynamic stable situations. Here we show the results for a set of buoyancy ratios $\{R_a = 0.075, R_b = 2.4, R_c = 1\}$ that produces dimensionless density profiles that match the experimental findings, *i.e.* the development of convective fingers as described above. The dimensionless density $\rho(a,b,c,\zeta)$ evolves from a stable stratification to a non-monotonic profile characterized by a maximum and a minimum symmetrically located across the line which initially separates the two layers. Eventually a monotonic shape with an absolute maximum in the upper layer is obtained. In the presence of the gravitational field, such a density configuration generates the convective scenario observed in the experiments (see Fig.2).

The density distribution along the gravitational axis also helps to understand the dependence of the cross-diffusion-induced instability upon the initial concentration gap, ΔC_0. The curves in Fig.6 describe the morphological variation of the density profile when C_0^B is increased from 0.1 to 1 M and the concentrations of A and B are fixed to 3.59 M and 0.299 M, respectively, where the microemulsions are structurally stable. Note that, in order to better appreciate the system response to these concentration changes, in Fig.6 we show the dimensional density profiles. Concentration and density dimensionless profiles are, by definition, renormalized over ΔC_0 and thus independent from variations in this parameter. Clearly a non-monotonic profile, characterized by a local mass accumulation above and a depletion zone below the initial interface, persists even if the density of the bottom layer is shifted to higher values. As explained in previous papers[29–32], similar non-monotonic profiles are typical of reactive and non-reactive two-layer miscible systems characterized by differential diffusivity. For instance, if a solution of a slow-diffusing solute 1 overlies a denser solution of a fast-diffusing species 2, a locally unstable density stratification will develop over time[31]. In these instability scenarios, when the density barrier below the interface increases, the characteristic time scale for the onset of the hydrodynamic instability increases and, conversely, convective motions are less intense, as the density extrema responsible for convective motions progressively decrease along the global density profile[33].

In our experimental investigations we found a decreasing trend for all the hydrodynamic parameters upon increasing the initial concentration of the salt in the bottom layer. At present it is difficult to give a full explanation for these trends, because the exact dependence of the cross-diffusion coefficients upon [$NaBrO_3$] must be known. In fact, according to our model, two opposite factors are at play in our system. The increment of C in the bottom layer both increases the density of the solution (stabilizing effect) and at the same time enhances cross-diffusive phenomena (destabilizing effect). For the set of parameters considered here $\{\delta_{ii}, \delta_{ij}, R_i\}$, the system results intrinsically unstable and, in our model, independent from ΔC_0. The parameters which characterize the instability dynamics are related with the ratio between the difference of density across the interface (density maximum and minimum above and below the interface, respectively) and the initial density difference between the top and the bottom layer[33]. In our model this ratio remains constant while increasing ΔC_0, being the latter a proportional factor for both terms. However, Figure 6 shows an enhancement of the density barrier below the density minimum in the lower layer, which restrains the downward finger displacement and explain the asymmetric growth rate along the upward and downward direction found in the experiments (see Figure 2f). This also explains the decreasing trend of l_m and v_m reported in Figure 4. In order to account for the behavior of t_0 and λ_m exact measurements of the dependence of cross-diffusion coefficients D_{13} and D_{23} upon [$NaBrO_3$] are in progress, and their inclusion in a more detailed model will be the subject of a forthcoming paper.

Within our theoretical framework we can predict a hydrodynamic stabilization of the system by replacing the salt in the bottom layer with a species characterized by a larger solutal expansion coefficient which, even with similar cross-diffusion effects on the other species, prevents the formation of non-monotonic density distributions. In this way, in fact, we can increase the density of the bottom layer without triggering any cross-diffusive transport due to concentration effects.

5 Conclusion

In ternary and quaternary microemulsion systems, cross-diffusion coefficients can be much larger than the diagonal terms of the diffusion matrix, *i.e.*, the motion of one solute along its concentration gradient causes a flux of the other solutes either along (*co*-flux, positive cross-diffusion sign) or against (*counter*-flux, negative sign) that concentration gradient. We have shown here that microemulsions feature a novel system where cross-diffusion-driven hydrodynamic instabilities can occur. Cross-diffusion is able to destabilise a homogeneous solution of microemulsion with regard to convective fingering, provided that a concentration gradient of an additional species is initially present in the system. Specifically, if two identical water/AOT microemulsions are in contact in a vertical Hele-Shaw cell, the interface between them can be destabilised because of a buoyancy-driven instability when the lower solution contains a simple water-soluble molecule triggering positive cross-diffusion. By pulling the other species along its upward transport, the motion of this unreactive molecule induces the build-up of a non-monotonic density profile in time and hence the onset of convection. We showed here the behavior for $NaBrO_3$, for which the diffusion matrix is known, but similar results were obtained in experiments were the water-soluble species was either $KMnO_4$ or $K_2Cr_2O_7$. We studied the properties of the related convective fingers experimentally and explained their characteristic by a cross-diffusion model. Work is in progress to explore new scenarios in which the chemical species experience a negative cross-diffusive interplay. A key step for a deep understanding of these phenomena is to elucidate the actual effect of local concentration on the cross-diffusion terms and, hence, in the hydrodynamic instabilities.

Our results open perspectives in the study of cross-diffusion driven RDC patterns in microemulsions. Indeed, the H_2O/AOT/octane system is well known to yield numerous RD patterns when oscillatory chemical reactions are dispersed in the microemulsion nanodroplets. In these systems, cross-diffusion effects certainly play a role in the pattern selection and evolution. The replacement of the inert salt used here by a full set of chemical species reacting in the micellar environment is thus likely to increase the variety of pattern-forming instabilities by a synergy between RD and convective instability mechanisms.

Acknowledgments

F.R. was supported by grants "Fondo Giovani Ricercatori 2012" and "ORSA120144" (FARB ex 60%) funded by the

University of Salerno. L.L. acknowledges support from FRIA. M.A.B. gratefully acknowledges Regione Sardegna for financial support in the framework of “Asse IV Capitale Umano, Obiettivo Operativo l.3 Linea di Attività l.3.1 del P.O.R. Sardegna F.S.E. 2007/2013 - Progetti in forma associata e/o partenariale C.U.P. E85E12000060009”. A.D. acknowledges financial support from Prodex and from the FRS-FNRS project “FORECAST”. We gratefully acknowledge Prof. Irving Epstein for reading the manuscript and for his valuable suggestions.

References

1 E. P. Zemskov, K. Kassner and M. J. B. Hauser, *Phys. Rev. E*, 2008, **77**, 036219–6.
2 V. K. Vanag and I. R. Epstein, *Phys. Chem. Chem. Phys.*, 2009, **11**, 897–912.
3 E. P. Zemskov, V. K. Vanag and I. R. Epstein, *Phys. Rev. E*, 2011, **84**, 036216.
4 E. P. Zemskov, K. Kassner, M. J. B. Hauser and W. Horsthemke, *Phys. Rev. E*, 2013, **87**, 032906.
5 I. Berenstein and C. Beta, *J. Chem. Phys*, 2012, **136**, 034903.
6 I. Berenstein and C. Beta, *Chaos*, 2013, **23**, 033119.
7 F. Rossi, V. K. Vanag and I. R. Epstein, *Chem. Eur. J.*, 2011, **17**, 2138–2145.
8 V. K. Vanag and I. R. Epstein, *Phys. Rev. Lett.*, 2001, **87**, 228301–4.
9 D. Leaist and L. Hao, *J. Phys. Chem.*, 1995, **99**, 12896–12901.
10 D. G. Leaist, *Phys. Chem. Chem. Phys.*, 2002, **4**, 4732–4739.
11 V. K. Vanag, F. Rossi, A. Cherkashin and I. R. Epstein, *J. Phys. Chem. B*, 2008, **112**, 9058–9070.
12 F. Rossi, V. K. Vanag, E. Tiezzi and I. R. Epstein, *J. Phys. Chem. B*, 2010, **114**, 8140–8146.
13 B. N. Preston, T. C. Laurent, W. D. Comper and G. J. Checkley, *Nature*, 1980, **287**, 499–503.
14 T. C. Laurent, B. N. Preston, W. D. Comper, G. J. Checkley, K. Edsman and L. O. Sundelof, *J. Phys. Chem.*, 1983, **87**, 648–654.
15 W. D. Comper, G. J. Checkley and B. N. Preston, *J. Phys. Chem.*, 1984, **88**, 1068–1076.
16 W. D. Comper, G. J. Checkley and B. N. Preston, *J. Phys. Chem.*, 1985, **89**, 1551–1555.
17 W. D. Comper, R. P. W. Williams, G. J. Checkley and B. N. Preston, *J. Phys. Chem.*, 1987, **91**, 993–1000.
18 H. Maeda, T. Mashita, H. Ojima, S. Sasaki, Y. Tomita, T. Fukuda and M. Yamanaka, *J. Phys. Chem.*, 1994, **98**, 13426–13431.
19 H. Maeda, S. Sasaki, T. Mashita, K. Nakamura, H. Ojima, T. Gotoh, T. Fukuda and M. Yamanaka, *J. Mol. Liq.*, 1995, **6566**, 341–344.
20 H. Maeda, K.-i. Nakamura, H. Yamane, S. Sasaki and R. Kakehashi, *Colloids Surf. A-Physicochem. Eng. Asp.*, 2014, **440**, 131–135.
21 S. Sasaki, *J. Phys. Chem.*, 1996, **100**, 20164–20171.
22 E. L. Cussler, *Diffusion: mass transfer in fluid systems*, Cambridge University Press, Cambridge; New York, 2009.
23 A. K. Ganguli, A. Ganguly and S. Vaidya, *Chem. Soc. Rev.*, 2010, **39**, 474–485.
24 M. Almgren and R. Johannsson, *The Journal of Physical Chemistry*, 1992, **96**, 9512–9517.
25 P. L. Luisi, M. Giomini, M. P. Pileni and B. H. Robinson, *Biochimica et Biophysica Acta (BBA) - Reviews on Biomembranes*, 1988, **947**, 209–246.
26 T. K. De and A. Maitra, *Advances in Colloid and Interface Science*, 1995, **59**, 95–193.
27 Y. Shi and K. Eckert, *Chem. Eng. Sci.*, 2008, **63**, 3560.
28 L. Joannes, F. Dubois and J.-C. Legros, *Appl. Opt.*, 2003, **42**, 5046.
29 P. M. Trevelyan, C. Almarcha and A. De Wit, *J. Fluid Mech.*, 2011, **670**, 3865.
30 C. Almarcha, P. Trevelyan, P. Grosfils and A. De Wit, *Phys. Rev. Lett.*, 2010, **104**, 044501.
31 L. Lemaigre, M. Budroni, L. Riolfo, P. Grosfils and A. De Wit, *Phys. Fluids*, 2013, **25**, 014103.
32 C. Almarcha, Y. R’Honi, Y. De Decker, P. Trevelyan, K. Eckert and A. De Wit, *Phys. Fluids*, 2011, **25**, 9739.
33 S. Kuster, L. Riolfo, A. Zalts, C. E. Hasi, C. Almarcha, P. Trevelyan, A. De Wit and A. D’Onofrio, *Physical Chemistry Chemical Physics*, 2011, **13**, 1795.